journal

J. Am. Ceram. Soc., 97 [7] 2038–2045 (2014)
DOI: 10.1111/jace.12970

Quantitative Texture Analysis of Spark Plasma Textured n-Bi_2Te_3

Quentin Lognoné,[‡] Franck Gascoin,[‡,†] Oleg I. Lebedev,[‡] Luca Lutterotti,[‡,§,¶] Stéphanie Gascoin,[‡] and Daniel Chateigner[‡,§]

[‡]Laboratoire CRISMAT UMR 6508 CNRS ENSICAEN, 6 boulevard du Maréchal Juin, Caen Cedex 04 14050, France

[§]IUT-Caen, Université de Caen Basse-Normandie, 6 boulevard du Maréchal Juin, Caen 14050, France

[¶]Department of Industrial Engineering, University of Trento, via Mesiano, 77, Trento 38050, Italy

For the first time, the quantitative texture analysis of edge free sintered $Bi_2Te_{2.4}Se_{0.6}$ samples elaborated by high-energy ball milling and Spark Plasma Texturing is performed. As expected, due to the structural anisotropy, the forging process results in a significant decrease in electrical resistivity perpendicularly to the uniaxial stress field. Surprisingly, this also leads to a large decrease in the lattice thermal conductivity in this direction. Crystallite boundaries amorphization as evidenced by transmission electron microscopy explains this latter decrease due to the friction induced by the applied pressure and grains sliding on each other during reorientation. X-ray diffraction also evidences development of strong crystallite size anisotropy and more isotropic microstrain developments under pressure, simultaneously favoring electronic conduction and phonon scattering, respectively. The thermoelectric performance is thus increased, however, the quantitative texture analysis demonstrates that the enhanced texture is only slightly responsible for the improved performance that rather comes from a peculiarly engineered microstructure.

I. Introduction

Doped bismuth telluride (Bi_2Te_3) still remains the best thermoelectric materials for near room-temperature applications, and even if it is already commercially available, efforts are still devoted toward the improvement of its thermoelectric performances. One way to obtain such improvement is via nanostructuring, hence targeting the lowering of the thermal conductivity by an increased phonon scattering generated by the multiplication of the grain boundaries or interfaces throughout the bulk material.[1–3] An important feature of Bi_2Te_3, due to its layered structure, is its rather strong anisotropy in transport properties, giving rise to thermoelectric performances of *p*- and *n*-type doped Bi_2Te_3 larger along the *ab* plane than any other crystal direction.[4–7] Consequently, in a polycrystalline sample, it is possible to modify the macroscopic transport properties by controlling the degree of crystallographic preferred orientations of the constitutive crystals, and for randomly oriented crystals (random sample), the sample exhibits average transport properties. However, concerning thermoelectric efficiency, an increase in electrical conductivity due to texturing, is expected to be accompanied by a correlative rise of the thermal conductivity due to its electronic contribution, direct consequence of the Wiedemann Franz law.[8]

Uniaxial hot pressing of anisotropically shaped crystals similar to lamellar structures is known to promote the orientation with platelets aligned perpendicularly to the axis of pressure.[9,10] Furthermore, if during this process the material is allowed to flow freely in the direction perpendicular to the axis of pressure, the hot pressing becomes a hot forging or Spark Plasma Texturing[11–13] and the alignment of the grains can be optimized.

Combining high-energy ball milling and direct-current-induced uniaxial hot pressing is now recognized as a method to improve the thermoelectric figure of merit of existing thermoelectric materials.[1,3,9,14] This improvement is believed to come from an enhanced texture and from the increased phonon scattering by grain boundaries and structural defects. In this work, we show that the hot-forging process leads to a large increase (about 50%) in the electrical conductivity perpendicularly to the loading axis, whereas neither the Seebeck coefficient nor the thermal conductivity is significantly affected along this direction. This evidently leads to a 50% increase in the thermoelectric figure of merit. More importantly, we demonstrate that the enhanced texture is not responsible for this improvement. Rather, crystallite boundaries' (CBs) amorphization after the second hot pressing is responsible for this large increase, keeping relatively small thermal conductivities, together with severe crystallite morphology evolution and grain growth that enhance electrical conductivity. This simple elaboration route might potentially offer a way to significantly increase thermoelectric performances of a large variety of materials.

II. Experimental Procedure

Bismuth selenido-telluride samples were elaborated from pure elemental precursors (Alfa Aesar, Schiltigheim, France) of bismuth (needles, 99.99%), tellurium (shots, 99.99%), and selenium (shots, 99.99%). Appropriate stoichiometric mixture of the elements were loaded in a 20 mL tungsten carbide ball mill jar, containing seven tungsten carbide 10-mm-diameter balls. The mixture was then subjected to mechanical alloying for 30 min divided in 15 cycles of 2 min each at 700 rpm in a Fritsch Pulverisette 7 (Fritsch Gmbh, Idar-Oberstein, Germany) premium line device. The obtained powder was compacted a first time using spark plasma sintering (SPS) process in a graphite die of 15 mm diameter at a pressure of 25 MPa during 30 min at a temperature of 723 K. The resulting cylinder (SPS1) showed a density larger than 95% of the theoretical density and a thickness of about 15 mm. A piece was cut from the whole puck for analysis and transport property measurements. The rest of the puck was then re-pressed a second time, using the same pressure-temperature conditions, in a 20-mm-diameter graphite die which allowed a free lateral deformation of the pellet. After this second pressing step, the sample (SPS2) retained a density larger than 95% and a thickness of about 7 mm. Noteworthy, the

X.-D. Zhou—contributing editor

Manuscript No. 34014. Received October 28, 2013; approved March 24, 2014.
†Author to whom correspondence should be addressed. e-mail: franck.gascoin@ensicaen.fr

density above 95% of both SPS1 and SPS2 is indeed a prerequisite condition that allows the direct comparison of the thermal and electrical transport properties of the material after the first and the second densification cycle.

Texture, coherent domain sizes and shapes, microstrains, and structural variations were investigated using X-ray diffraction. We used a four-circle diffractometer setup equipped with a Curved Position Sensitive detector (CPS120 from INEL SA, Artenay, France), using the monochromatized CuK_α average radiation.[15] Data were analyzed within the combined analysis formalism[16] implemented in the MAUD software.[17] Briefly, this methodology allows the quantitative texture determination of the samples, using a cyclic Rietveld refinement of a series of X-rays diagrams measured at different sample orientations. It is then able to incorporate the determination of other sample features like structure, residual stresses, crystallite size and microdistortions, phase analyses, etc. Due to the relatively low expected texture strength in such samples, we measured 2Θ diagrams using a regular 5° × 5° grid in tilt and azimuth angles (χ and ϕ, respectively) with $0° \le \chi \le 55°$ and $0° \le \phi \le 355°$. It resulted in 864 diagrams, each one exhibiting nearly 4000 measured points. We used an incident angle of the X-ray beam on the sample plane of ω = 20°, approximately centered on the main Bragg peaks range for the phases of concerns, to reduce, on an average, the blind areas on these peaks.[16] The obtained pole figures are normalized into multiples of a random distribution (m.r.d.), a unit that does not depend on other factors than orientation. In such units, a sample without preferred orientations exhibits uniform pole figures with 1 m.r.d. levels, whereas a textured sample shows pole figures with maxima and minima of orientation densities ranging from 0 m.r.d. (absence of crystals oriented in this direction) to infinity (for a single crystal on few directions). The overall texture strength is evaluated through the texture index[18] which is expressed in m.r.d.^{2} units and varies from one (random powder) to infinity (perfect texture or single crystal) and used to compare the texture strength of different samples exhibiting similar Orientation Distributions (OD). Such normalized pole figures are calculated from the OD of crystallites, refined using the E-WIMV algorithm[19] after extraction of the peak intensities during the Rietveld cycles. The OD and profile refinement reliabilities are estimated using conventional reliability factors.[20] During these refinements, the unit-cell definition of bismuth telluride used is the R-3 m:H space group, Crystallography Open Database n° 1 511 976.[21] The sample reference frame is given by the SPS direction of pressure, P_{SPS}, which corresponds to the centers of the pole figures (Z). We could not detect any residual strains within our experimental resolution, that is, the residual stresses, if existing, are estimated lower than 10 MPa. Crystallite sizes, shapes, and microstrains were refined within the Rietveld cycles using the Popa description.[22] We estimate that our X-ray Combined Analysis setup probed several millions of crystallites. The instrument contributions (χ and ω broadenings, peak shapes, zero-shifts, line shapes, etc) were calibrated using the 660b LaB_6 powder standard from National Institute of Standards and Technology. A counting time of 2 min for each sample orientation was used, and our optical setup provides a 0.1° peak widths in 2θ around 2θ = 40°.

The OD and 2nd rank single crystal property tensors were then used to calculate the macroscopic tensor properties, electrical resistivity, thermal conductivity, and Seebeck coefficient [$\rho^M{}_{ij}$, ($\kappa^M{}_{ij}$, and $\alpha^M{}_{ij}$, respectively], using the geometric mean approach.[23] This allows us to estimate the orientation effect on the anisotropic properties of the SPS1 and SPS2 samples from intrinsic values. For our space group, and for our compositions that do not show magnetic ordering, all the anisotropic tensor properties of concern here can be represented by two independent components:

$$\rho_{ij} = \begin{vmatrix} \rho_{11} & . & . \\ . & \rho_{11} & . \\ . & . & \rho_{33} \end{vmatrix}; \kappa_{ij} = \begin{vmatrix} \kappa_{11} & . & . \\ . & \kappa_{11} & . \\ . & . & \kappa_{33} \end{vmatrix};$$

$$\alpha_{ij} = \begin{vmatrix} \alpha_{11} & . & . \\ . & \alpha_{11} & . \\ . & . & \alpha_{33} \end{vmatrix}$$

the axis 3 being parallel to the *c* axis of the structure and 1 perpendicular to it. Considering the measured carrier concentration of our samples, we used the single crystal tensors determined by Scherrer *et al.*[7,24] [tables 10 and 12, $n = 5.7 \times 10^{19}$ cm^{-3}], that is, $\rho_{11} = 9.8$ μΩ·m, $\rho_{33} = 54$ μΩ·m, $\kappa_{11} = 1.70$ W·(m·K)$^{-1}$, $\kappa_{33} = 0.75$ W·(m·K)$^{-1}$, $\alpha_{11} = 207$ μV/K, and $\alpha_{33} = 195$ μV/K.

The macroscopic resistivity and Seebeck coefficients ($\rho^M{}_{11}$ and $\alpha^M{}_{11}$ resp.) were measured in a direction perpendicular to P_{SPS} with an ULVAC ZEM-3 apparatus using the four-point probe method and differential (ULVAC, Tokyo, Japan) method, respectively. Measurements were made on 2 mm × 2 mm section and 10-mm-length bars between 300 and 473 K under a partial pressure of 0.1 atm of helium. The $\Lambda^M{}_{11}$ thermal diffusivity (also measured perpendicularly to P_{SPS}) was determined by flash laser method using a LFA457 device (Netzsch, Selb, Germany), under 20 mL per min nitrogen flow. Samples were 6 mm × 6 mm squares with a thickness of 1 mm. Samples' heat capacity was calculated within the Dulong–Petit approximation and used for the determination of the macroscopic thermal conductivity $\kappa^M{}_{ij}$. The bulk density was measured by Archimedes method using ethanol as the displaced fluid. Microstructures were examined on fractured samples by using a Carl Zeiss scanning electron microscope (SEM).

Transmission electron microscopy (TEM), electron diffraction (ED), and high resolution TEM (HRTEM) studies were carried out using a FEI Tecnai G2 30 UT microscope (Tecnai, Eindhoven, the Netherlands) operated at 300 kV and having 0.17 nm point resolution. The chemical composition of the material was verified by EDX analysis using an energy-dispersive X-ray analysis attached system. Two types of cross-sectional specimens were prepared for TEM experiments using conventional specimen preparation technique. To have 3D information on crystallites and CB's structure, the cross-sectional samples were cut parallel and perpendicular to P_{SPS}, mechanically polished to the thickness of about 50 μm and finally Ar^+ ion-beam milled under grazing incidence with respect to the surface by using a JEOL Ion Slicer machine (JEOL, Tokyo, Japan). It is important to notice that ion-milling was carried out with the same conditions for both SPS samples (SPS1 and SPS2). This allows for proper TEM comparative analysis of the structure of the two samples.

III. Results and Discussion

Figure 1 shows the SEM images of fractured pieces of SPS1 and SPS2 in a plane parallel (left images) and perpendicular (right images) to P_{SPS}. Two features appear on this figure, that is, (1) grain growth promotion by the 450°C temperature [comparing Figs. 1(a) and (c), or 2(b) and (d)] needed to insure densification in a platelet-like shape; and (2) enhanced platelets alignment with short dimension of the platelets tending to align with P_{SPS}. Noteworthy, the SEM grain size is roughly ten times larger in SPS2 than in SPS1, being extended typically from some micrometers in the latter to some 10 μm in the former. Such an increase in texture and grain sizes is expected to have a significant effect on the transport properties. In this contribution, because the elaboration process results in thin samples, all the transport measurements correspond to fluxes along the transverse direction, perpendicular to P_{SPS}, that is, the 1 or 2 macroscopic directions. From the Curie principle, it is not expected

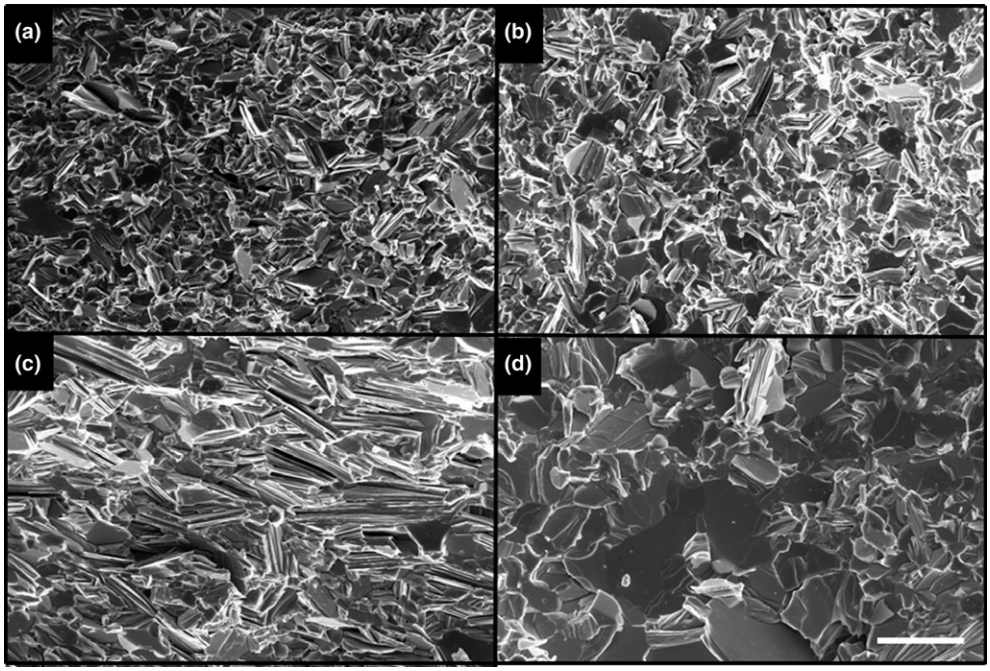

Fig. 1. Scanning electron microscopy images of fractured pieces of SPS1 and SPS2 in a plane parallel [(a) and (c) images] and perpendicular [(b) and (d) images] to P_{SPS} (scale bar = 10 μm).

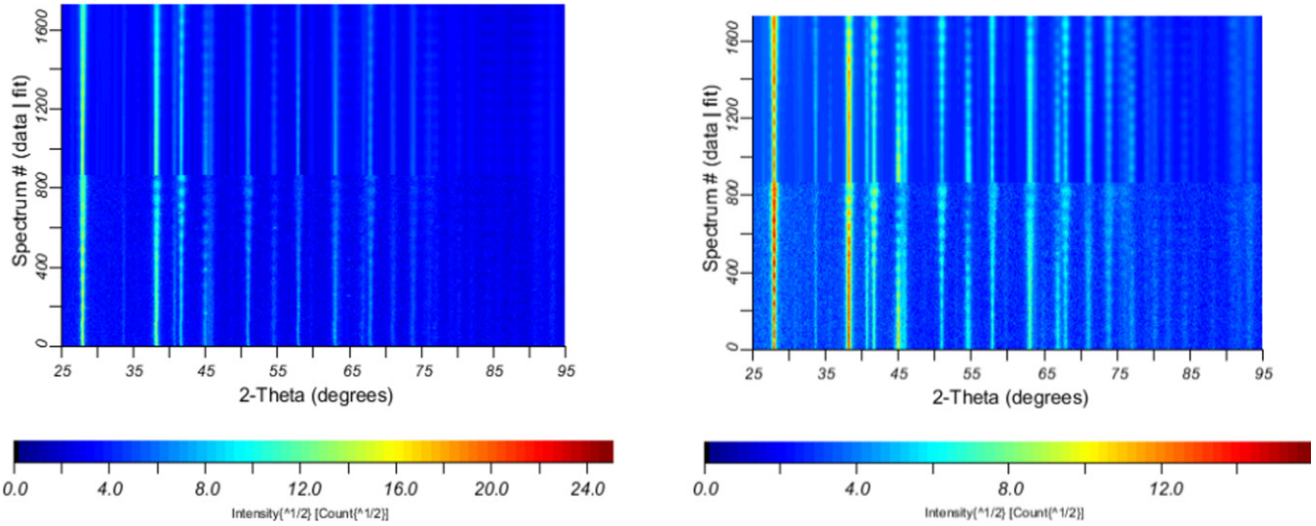

Fig. 2. X-ray diffraction diagrams measured for all the (χ, ϕ) orientations of the samples (bottom diagrams), and refined diagrams after Combined Analysis (bottom), showing the reproducibility of the methodology for both SPS1 (a) and SPS2 (b) samples.

any deviation from axial symmetry around P_{SPS}, and 1 and 2 directions should be equivalent.

Variations in diffracted intensities are observed with the (χ,ϕ) orientation of the SPS samples (Fig. 2, bottom diagrams), more pronounced on SPS2 as a sign of its stronger crystallographic texture. Combined analysis refinement (Fig. 2, top diagrams) correctly reproduces the experimental diagrams, with reliability factors Rw = 33.2%, Rexp = 26.3% and Rw = 31.6%, Rexp = 26.4% for SPS1 and SPS2, respectively. Such factors could appear large, however, one has to remember that reliability factors depend on the number of experimental points, which in our case is very large (around 2 million per sample) and should be compared to the complexity of the model. Considering these two factors one can evaluate a χ^2 value of 1.26 and 1.19, respectively, corresponding to good refinement values. The pole figures for the main crystallographic directions of $Bi_2Te_{2.4}Se_{0.6}$ (Fig. 3) are showing the preferred orientation stabilized in the two samples. Both samples exhibit fiber texture with fiber axis corresponding to the mean *c* axis of the structure. However, the fiber axis of SPS1 is inclined by about 40° from P_{SPS}, whereas in SPS2 this fiber axis has been reoriented to align with P_{SPS}. The maxima of the OD are of 4.3 and 45.1 m.r.d., respectively, the maxima in the {003} pole figures (1.7 and 4.5 m.r.d.), and the overall texture strength index F^2 of 1.01 and 3.9 m.r.d.^{2}, all pointing toward a relatively low texture strength, however, much more pronounced in SPS2. The ODs have been refined with the satisfactory reliability factors Rw = 14.8% and 14.4%, respectively, and show minima levels of 0 m.r.d. indicating that the orientation components are the only ones developed in our samples. The refinement converges to unit-cell parameters of $a = 4.32\,715(2)$ Å, $c = 30.1514(2)$ Å for SPS1 and $a = 4.32\,452(3)$ Å, $c = 30.1458(2)$ Å for SPS2, values that are coherent with the bulk ones for this phase as evidenced by the evolution of the cell parameters within the solid solution $Bi_2Te_{3-x}Se_x$ that clearly follows Vegard's law (Fig. 4).[25–30] We refined the *z* atomic positions (Table I) for Bi and Te(2) atoms and occupation factors of Te(1), constraining Se(1) to complement this latter site. These results do not show significant variations in the atomic positions between SPS1 and

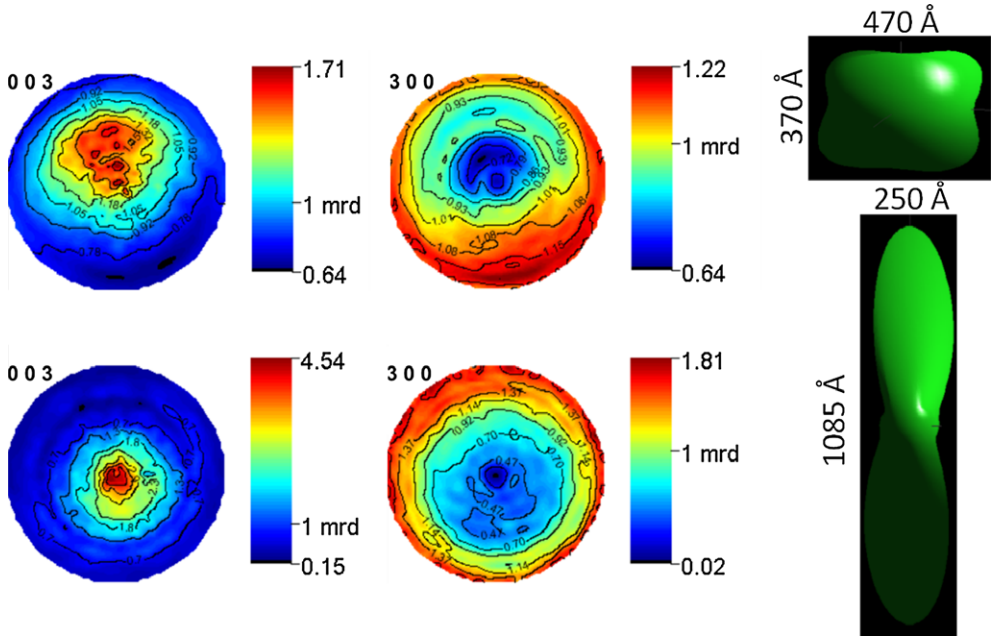

Fig. 3. {003} (left) and {300} (middle) pole figures and anisotropic mean crystallite shape (correct scale relative to each other) (right) for SPS1 (top) and SPS2 (bottom) recalculated from the combined analysis. Linear scales, equal area projections.

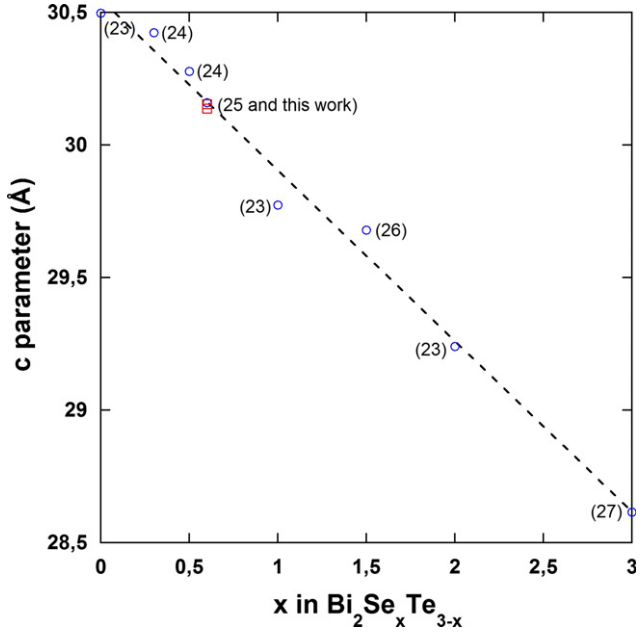

Fig. 4. Variation in the lattice parameter c with the content x of selenium in the compound $Bi_2Se_xTe_{3-x}$. Numbers in parentheses indicate the corresponding references.

Table I. Refined Structural Parameters of SPS1 and SPS2. In Parenthesis are the Standard Deviations on the Last Digit, as Refined within Combined Analysis

	SPS1		SPS2	
	z (Å)	Occupation	z (Å)	Occupation
Bi	0.39 780 (1)	1	0.39 824 (1)	1
Te(1)	0	0.79 (1)	0	0.838 (8)
Se(1)	0	0.21 (1)	0	0.162 (8)
Te(2)	0.21 118 (1)	1	0.21 145 (1)	1

SPS2, and the refined Se(1) occupations, though tending to poke for a small Se lost in SPS2, remain in agreement with the nominal composition of our samples. For all properties of concerns here, we are not expecting large influences from these latter differences in our case.

Astonishingly, the refined anisotropic mean crystallite sizes (Fig. 3), starting from 370 Å along the *c* axis and 470 Å along the a axis in SPS1, elongate by 2.5 times along *c* (1085 Å) but shrink by around 45% (250 Å) along a in SPS2. Comparing the SEM images of Fig. 1(c) with these latter sizes, and taking account of Fig. 3, the $Bi_2Te_{2.4}Se_{0.6}$ platelets which developed under the SPS2 conditions are made up with approximately two crystallites along their small dimension, whereas 400 coherent domains are present along the platelets' long dimension, that is, as an average perpendicularly to P_{SPS}. We would then expect a quite different behavior along P_{SPS} and transversally. We could not evidence significant differences between the two samples mean microstrain levels, of about 7.10^{-4} rms.

Taking account of the single-crystal constants of $Bi_2Te_{2.4}Se_{0.6}$ and the refined OD of the two samples, we obtained the following macroscopic tensors:

$$\rho_{ij}^{M} = \begin{vmatrix} 17.31 & . & . \\ . & 17.31 & . \\ . & . & 17.32 \end{vmatrix};$$

$$\kappa_{ij}^{M} = \begin{vmatrix} 1.32 & . & . \\ . & 1.29 & . \\ . & . & 1.27 \end{vmatrix}; \alpha_{ij}^{M} = \begin{vmatrix} 203 & . & . \\ . & 203 & . \\ . & . & 202.7 \end{vmatrix}$$

for SPS1 and,

$$\rho_{ij}^{M} = \begin{vmatrix} 16.79 & . & . \\ . & 16.79 & . \\ . & . & 18.39 \end{vmatrix};$$

$$\kappa_{ij}^{M} = \begin{vmatrix} 1.32 & . & . \\ . & 1.32 & . \\ . & . & 1.25 \end{vmatrix}; \alpha_{ij}^{M} = \begin{vmatrix} 203.2 & . & . \\ . & 203.2 & . \\ . & . & 202.4 \end{vmatrix}$$

for SPS2,

from which we can calculate the anisotropy factors between the 3 and 1 directions of the samples (Table II).

Table II. Anisotropy Factors Between the 3 and 1 Directions of our Samples, as Calculated from the Refined Macroscopic Tensors

	$\rho^{M}_{33}/\rho^{M}_{11}$	$\kappa^{M}_{33}/\kappa^{M}_{11}$	$\alpha^{M}_{33}/\alpha^{M}_{11}$
Single crystal[5]	5.51	0.44	0.94
SPS1	1.00	0.97	1.00
SPS2	1.10	0.95	1.00

As expected from the relatively low texture strengths, the anisotropies in main macroscopic properties due to orientation effects (the sole ones evaluated quantitatively at this stage) are not pronounced, or even absent for the macroscopic Seebeck coefficient. This is also due to the fiber character of the texture which tends to homogenize physical properties. Sample SPS1 appears to behave as perfectly isotropic in all properties of concerns. However, the anisotropy in both thermal conductivity and electrical resistivity are somewhat larger in SPS2 (by 5% and 10%, respectively), and other parameters extrinsic to the crystallites might induce other anisotropic effects, such as grain-boundary densities linked to the anisotropic crystallite sizes.

Figure 5 shows the variation in the electrical resistivity of SPS1 and SPS2 samples with temperature. A large decrease in about 35% of the electrical resistivity along the 1-direction is observed from SPS1 to SPS2. This latter can be partially explained by the strong anisotropy of the electrical resistivity known to exist in *n* and *p* type bismuth telluride.[4–7] As Shown by Scherrer *et al.*,[7] depending on the carrier concentration, the ratio between the 1 and 3 directions for electrical resistivity is between 4 and 6 in single crystals of bismuth selenide-telluride.[7] Thus, it would be expected that a perfectly randomly oriented sample would exhibit resistivities such that $\rho^{M}_{11} = \rho^{M}_{22} = \rho^{M}_{33}$. In our study, the increased texture due to the second hot pressing, has a direct influence on the electrical resistivity, however, as shown by our macroscopic tensor calculations (Table II), the effect of orientation is not attempted to be strong, the relative electrical resistivity decrease (comparing SPS2 to SPS1) being not larger than 3% along the 1-direction. This tends to prove that this anisotropy enhancement rather comes from grain boundary (GB) effects, that is, morphological texture: the GB density along P_{SPS} is larger than perpendicularly (Fig. 1), increasing the macroscopic resistivity much more along its 33 component as evidence by the larger value of ρ^{M}_{33}(SPS2), whereas CBs have only weak effect on the resistivity.

As for the Seebeck coefficient, it is known to be almost isotropic in bismuth telluride single crystal, and indeed, as shown on Fig. 5 and Table II, SPS1 and SPS2 exhibit virtually the same thermopower value, that is, the one of an isotropic sample, and variation with temperature. This also tends to indicate that the carrier concentration remains constant from SPS1 to SPS2, precluding any donor-like effect that could have been engendered by the multiple hot pressing.

The electrical resistivity decrease from SPS1 to SPS2 has a direct impact on the thermal conductivity as its electronic contribution (κ^{M}_{11el}) will increase in the same proportion which is in accordance with the Weidemann–Franz law.[8] Moreover, as the second cycle of hot pressing causes a clear grain growth, the lattice contribution to the thermal conductivity (κ^{M}_{11lat}) should increase due to a decreased number of grain boundaries resulting in lower phonons scattering. The total thermal conductivity of SPS1 and SPS2 (Fig. 5), however, remains almost identical on the whole probed temperature range. Even more surprisingly, as the electronic contribution of the thermal conductivity increases correlatively to the electrical resistivity decrease, it is thus the lattice contribution to the thermal conductivity that has decreased in SPS2, in direct opposition to the fact that the grains are bigger in this latter than in SPS1. This behavior is often justified by the presence of nanometer-size defects or nanodomains[1,30,31] whose formation is promoted by the ball-milling technique used to prepare the alloys. However, even if this nanostructuring effect had an impact, it should be more pronounced for SPS1 than for SPS2 as the latter has undergone a second heat treatment. As this is not the case, it is very debatable to suggest that such a nanostructuring can be accounted for the difference in thermal transport properties observed between our samples.

This striking behavior leads to a thermoelectric figure of merit zT^{M}_{11} (Fig. 6) that increases by as much as 50% from SPS1 to SPS2, almost reaching 1 at 425 K. But, more than the absolute value of the zT, the way it has been increased must be stressed out and discussed. Indeed, it is in direct contradiction with the general idea of nanostructuration

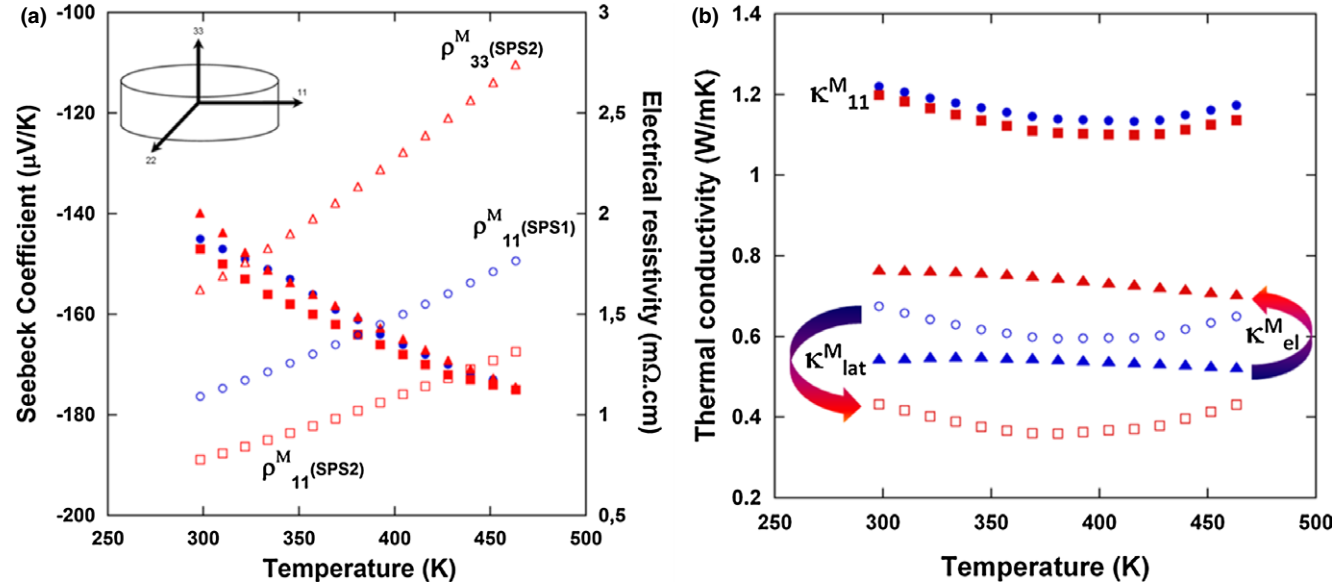

Fig. 5. Evolution of the transport properties of SPS1 (in blue) and SPS2 (in red) as a function of temperature. (a) Electrical resistivity (empty labels) and Seebeck coefficient (filled labels). (b) total thermal conductivity κ^{M} (filled circles and squares), electronic contribution κ^{M}_{el} (filled triangles), and lattice contribution κ^{M}_{lat} (empty circles and squares). The electronic contribution of the thermal conductivity is calculated as $\kappa_{el} = LT\sigma$ where, L is the Lorenz factor (chosen as equal to 2×10^{-8} $W\Omega/K^2$), T is the absolute temperature, and σ is the measured electronic conductivity.

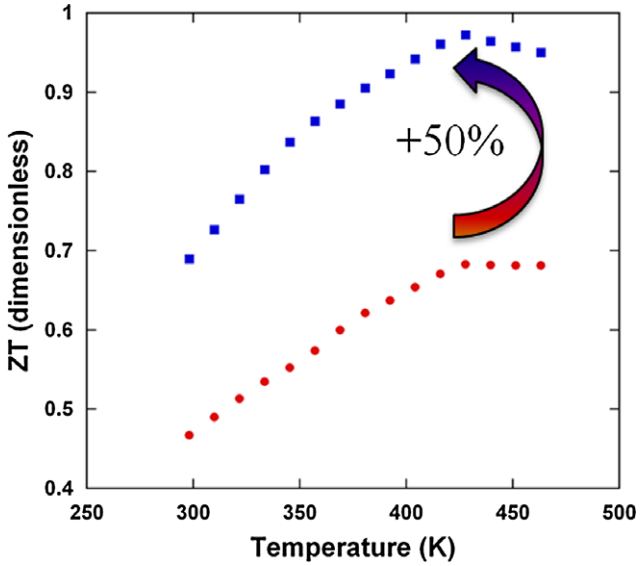

Fig. 6. Evolution of the thermoelectric figure of merit zT^{M}_{11} of SPS1 (blue) and SPS2 (red) as a function of temperature demonstrating the 50% increased solely due to the second sintering cycle.

commonly used as a mean to increase the number of grain boundaries and interfaces to scatter more efficiently the phonons.[1–3] Here, the visible increase in grain size from SPS1 to SPS2 does not lead to an increasing κ^{M}_{11lat}. On the contrary, this latter decreases by a factor of 2–2.5 from SPS1 to SPS2 [Fig. 4(b)], astonishingly. To clarify this behavior, meticulous examination of the crystallites boundaries (CB hereafter) at smaller scales has been performed using TEM.

TEM images (Fig. 7) clearly demonstrate the differences in the CB structure between SPS1 and SPS2 samples. In SPS1, all observed CB exhibit sharp, flat and free of secondary phase interfaces. A low-magnification image of 90-degree rotated grains of SPS1 is shown in Fig. 7(a). The boundary corresponds to a (01-1) plane, fairly well localized and no intermediate layer can be observed at the boundary between the two crystallites. A HRTEM image of another CB in SPS1 [Fig. 7(b)] evidences the absence of any intermediate layers and/or secondary phase. The ED pattern can be indexed on the basis of the rhombohedral $Bi_2Te_{3-x}Se_x$ phase indexed in the hexagonal unit-cell (R-3 m:H, a = 4.298 Å, c = 29.774 Å COD # n° 1 511 976) as consistently with XRD data. The composition was also confirmed by EDX measurements and is in good agreement with the nominal composition. Obviously, no amorphous layer, intermediate or secondary phases are present at the grain boundary. The structure of CB's in the SPS2 sample is neatly different as illustrated on representative low-magnification bright-field TEM images [Fig. 7(c)]. The boundary between the two shown crystallites is not anymore straight and flat. Moreover, a bright contrast layer appears along the boundary. A HRTEM image of the CB confirms the presence of an intermediate layer at the bright layer of the grain boundary. The thickness of this layer is quite uniform and is of the order of ~2 nm. As the CB is not flat and straight, and the TEM observation is a projection onto an image plane, the image of the boundary is often a superposition of two lattices. This makes the straightforward analysis of the TEM

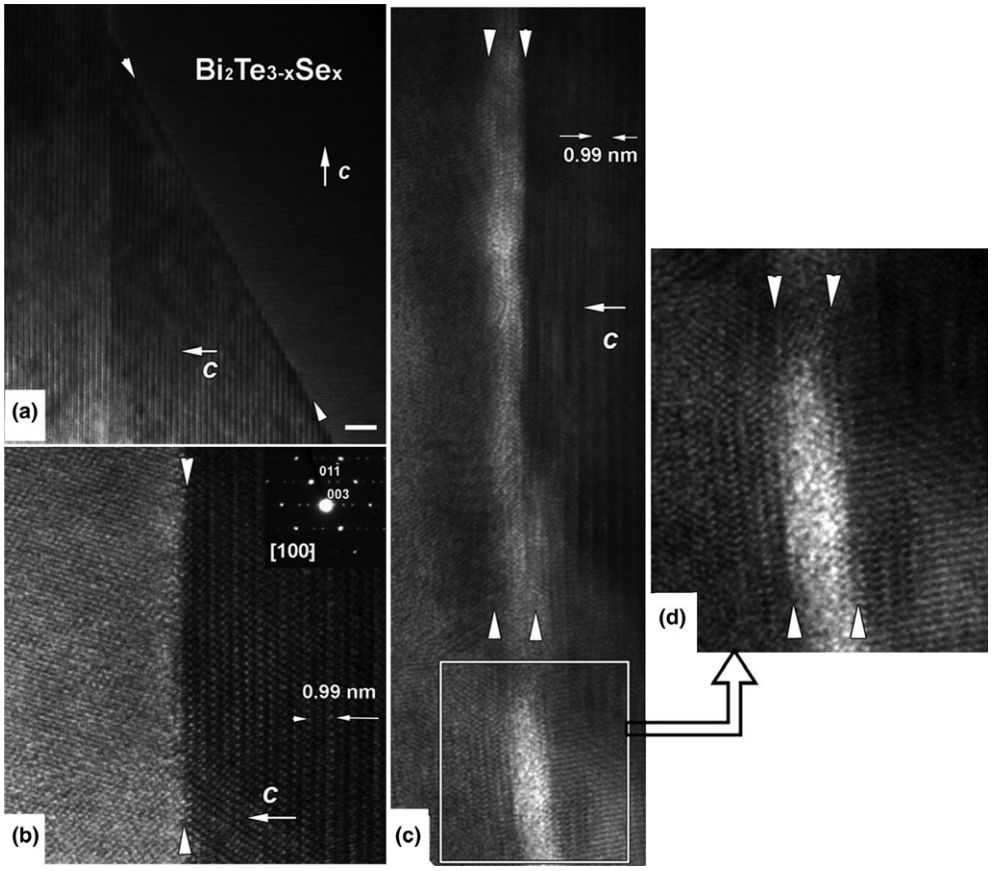

Fig. 7. TEM observation of the crystallite boundaries structure. TEM images of the crystallite boundaries (CB) in $Bi_2Te_{3-x}Se_x$ SPS1 (a, b) and SPS2 (c, d) samples. (a) Low-magnification bright-field TEM image of 90 degree rotated CB in SPS1 sample. The boundary is indicated by white arrowheads. Scale bar = 5 nm. (b) HRTEM image of CB between two differently oriented grains in SPS1 sample. Selected-area electron diffraction pattern is given as an insert and corresponds to [100] zone axis of $Bi_2Te_{3-x}Se_x$. (c) HRTEM image of typical CB found in SPS2. A layer of bright contrast along CB is indicated by pairs of white arrowheads. (d) Enlargement HRTEM image of selected by white rectangle in figure (c) area. Two pairs of white arrowheads indicated region of bright contrast layer in CB where no crystallite overlapping occurs.

images of the boundary and layer structure difficult. Nevertheless, depletion of the contrast at the interface is evident. Certainly, TEM image contrast can be produced by several different mechanisms and depends on image and specimens conditions, such as orientation, thickness, and defocus. However, within a single HRTEM measurement on a single crystal all these parameters can be considered equivalent and image contrast simply can be interpreted in term of absorption and diffraction contrasts. The absorption contrast depends on the fact that the elastic and inelastic scatterings of electrons increase with the atomic number. In this case the thicker area may consist of heavy atoms that will deplete the transmission beam more than lighter atoms, and appears darker in contrast. The diffraction contrast is produced by transmitted and diffracted electrons. In this case, if there are regions of the crystal where lattice planes are bent or where the structure is disordered, the diffracted intensity can be locally increased resulting, in appearance, in a brighter contrast compared with the surrounding areas. In this respect, taking into account the unlikely nonuniform thicknesses and chemical composition in the 2 nm interface layer we assume that observed bright contrast layers at the boundary are due to the presence of a disordered structure. This is also confirmed by an EDX mapping (performed under TEM) that shows the overall homogeneity of the samples without any compositional discrepancy at the CBs. In fact no stoichiometry difference could be found between SPS1 and SPS2, in good agreement with the refined lattice parameters (Fig. 4). Moreover, the mapping of SPS2 samples, performed over a surface that encompasses several crystallites boundaries, did not show any stoichiometry changes when passing through grains boundaries, comforting the idea of the formation of amorphous crystallites boundaries. Figure 7(d) shows an enlarged area of the CB selected by the white rectangle in Fig. 7(c). This part of the CB is clearly free of overlapping crystallites and this area provides a strong evidence of the presence of highly disordered (most probably amorphous) layer at the CBs and strongly supports our assumption. Interestingly, the typical distance between these disordered CB is in the range of the coherent size domains (crystallite sizes) determined by X-ray diffraction on SPS2 perpendicularly to P_{SPS}, that is, 25 nm.

The CB differences observed between SPS1 and SPS2, together with the fact that disordered CBs will contribute to an enlarged phonon scattering, explain the lowering of the lattice thermal conductivity $\kappa^{M}{}_{11lat}$ from SPS1 to SPS2. The origin of the degradation of these grain boundaries evidently comes from the second cycle of sintering. As the bismuth selenido-telluride grains are plate-like shaped, they have the tendency to be oriented perpendicular to the pressing direction. During the second sintering cycle, their reorientation is partly made possible because the used pressure forces the grains to glide on each others. This reorientation is, however, limited at solid state, and provokes intense frictions at the interfaces between grains, even reinforced by grain growth. This creates internal defects in the grains, visible as disordered/amorphous CBs. It may be proposed that the disordered CBs should also result in an increased electrical resistivity. However, the characteristic mean free path for phonons $_{p}$ in related materials has been evaluated to only some nm, that is, typically the size of the crystallite grain boundaries observed in SPS2, whereas the electron mean free path $_{e}$ in the parent phase Bi_2Te_3 is at least of 550 nm at 300 K, that is, about half the grain size along the (a, b) planes.[32,33] In the parent phase $_{e}$ decreases for larger temperatures,[33] giving rise to an increased electrical resistivity, which we also observe in our samples. The achievement of nanometer size CBs within several micrometers of grains allows then pronounced crystallite boundary and interface phonon scattering at the disordered interfaces created by the second sintering step, hereby decreasing thermal conductivity, whereas electrical resistivity remains small thanks to the conjugated effects of crystal growth and orientation.

IV. Conclusions

A quantitative texture analysis is performed for the first time on a hot-forged bismuth telluride alloys.

We have shown that by a careful control of sintering under SPS conditions the creation of both amorphous CBs, as seen locally using HRTEM or macroscopically using X-ray diffraction profile analysis, and significant grain growth and partial orientation, can be operated. This grain and CBs engineering allows an efficient way of reducing simultaneously the electrical resistivity—because of the presence of less grain boundaries perpendicularly to P_{SPS}—and the thermal conductivity—because more CBs are created perpendicularly to P_{SPS}—giving rise to a large improvement in zT. The texture analysis also reveals that the second sintering step does increase the degree of texture, however, this increase has a very limited effect (5% to 10%) on the macroscopic transport properties, indication that the thermoelectric performance improvement is rather mainly due to the abovementioned micro and nanostructure modifications.

These results have been reproduced several times and according to our results, further improvements are likely as the parameters of the sintering cycles (time and temperature) have an impact on grain size and degree of texture. Moreover, the same technique might be useful to improve the thermoelectric properties of various materials, the first targets might evidently be anisotropic materials but eventually even isotropic materials should be tested as the process is "simply" mechanical and results from the combined grain growth and amorphization of the crystallite boundary by friction, leading to a decreased lattice thermal conductivity.

Acknowledgments

The authors are indebted to L. Gouleuf for the TEM sample preparation. LL and DC would like to thank the Conseil Régional de Basse-Normandie and the Fond Européen de Développement Régional for co-financing LL's Chair of Excellence at CRISMAT-ENSICAEN, and partly financing the X-rays instruments.

References

[1]Y. Lan, A. J. Minnich, G. Chen, and Z. F. Ren, "Enhancement of Thermoelectric Figure of Merit by a Bulk Nanostructuring Approach," *Adv. Funct. Mater.*, **20** [35] 7–376 (2010).

[2]D. L. Medlin and G. J. Snyder, "Interfaces in Bulk Thermoelectric Materials," *Curr. Opin. Colloid Interface Sci.*, **14**, 226–35 (2009).

[3]K. S. Bux, J. P. Fleurial, and R. B. Kaner, "Nanostructured Materials for Thermoelectric Applications," *Chem. Commun.*, **46**, 8311–24 (2010).

[4]J. J. Shen, L. P. Hu, T. J. Zhu, and X. B. Zhao, "The Texture Related Anisotropy of Thermoelectric Properties in Bismuth Telluride Based Polycrystalline Alloys," *Appl. Phys. Lett.*, **99**, 124102 (2011).

[5]W. S. Liu, Q. Y. Zhang, Y. C. Lan, S. Chen, X. Yan, Q. Zhang, H. Wang, D. Z. Wang, G. Chen, and Z. F. Ren, "Thermoelectric Property Studies on Cu-Doped n-Type $Cu_xBi_2Te_{2.7}Se_{0.3}$ Nanocomposites," *Adv. Energy Mater.*, **1**, 577–87 (2011).

[6]L. Hu, H. Gao, X. Liu, J. Shen, T. Zhu, and X. Zhao, "Enhancement in thermoelectric performance of bismuth telluride based alloys by multi-scale microstructural effects," *J. Mater. Chem.*, **22**, 16484–90 (2012).

[7]H. Scherrer and S. Scherrer, "Bismuth Telluride, Antimony Telluride, and their Solid Solutions"; pp. 211–37 in *CRC Handbook of Thermoelectrics*, Edited by M. Rowe. CRC, Boca Raton, 1995.

[8]G. Weidemann and R. Franz, "Uber die Warme-Leitungsfahigkeit der Metalle," *Ann. Phys.*, **89**, 497–531 (1853).

[9]X. B. Yan, Y. Poudel, W. S. Ma, G. Liu, H. Joshi, Y. Wang, D. Lan, D. Z. Wang, G. Chen, and Z. F. Ren, "Experimental Studies on Anisotropic Thermoelectric Properties and Structures of n-Type $Bi_2Te_{2.7}Se_{0.3}$," *Nano Lett.*, **10**, 3373–8 (2010).

[10]E. Guilmeau, D. Chateigner, and J. Noudem, "Combined Analysis of Bi2223 Superconducting Bulk Materials," *Supercond. Sci. Tech.*, **15**, 1436–44 (2002).

[11]J. J. Shen, Z. Z. Yin, S. H. Yang, C. Yu, T. J. Zhu, and X. B. Zhao, "Improved Thermoelectric Performance of p-Type Bismuth Antimony Telluride Bulk Alloys Prepared by Hot Forging," *J. Electron. Mater.*, **40**, 1095–9 (2011).

[12]J. G. Noudem, D. Kenfaui, D. Chateigner, and M. Gomina, "Toward the Enhancement of Thermoelectric Properties of Lamellar $Ca_3Co_4O_9$ by Edge-Free Spark Plasma Texturing," *Scripta Mater.*, **66**, 258–60 (2012).

[13]L. P. Hu, X. H. Liu, H. H. Xie, J. J. Chen, T. J. Zhu, and X. B. Zhao, "Improved Thermoelectric Properties of n-Type Bismuth Telluride Based

Alloys by Deformation Induced Lattice Defects and Texture Enhancement," *Acta Mater.*, **60**, 4431–7 (2012).
[14]B. Poudel, Q. Hao, Y. Ma, Y. C. Lan, A. Minnich, B. Yu, X. Yan, D. Z. Wang, A. Muto, D. Vashaee, X. Y. Chen, J. M. Liu, M. S. Dresselhaus, G. Chen, and Z. F. Ren, "High Thermoelectric Performance of Nanostructured Bismuth Antimony Telluride Bulk," *Alloy. Sci.*, **320**, 634–8 (2008).
[15]M. Morales, D. Chateigner, L. Lutterotti, and J. Ricote, "X-ray Combined QTA Using a CPS Applied to a Ferroelectric Ultrastructure," *Mater. Sci. Forum*, **408–412**, 113–8 (2002).
[16]D. Chateigner, *Combined Analysis*. Wiley-ISTE, London, 2010, p. 496.
[17]L. Lutterotti, "Nuclear Instruments and Methods in Physics Research B Total Pattern Fitting for the Combined Size–Strain–Stress–Texture Determination in Thin Film Diffraction," *Nucl. Instrum. Methods Phys. Res., Sect. B*, **268**, 334–40 (2010).
[18]S. Matthies, G. Vinel, and K. Helming, "Standard Distributions in Texture Analysis"; p. 449, Akademie-Verlag, Berlin, 1987.
[19]L. Lutterotti, D. Chateigner, S. Ferrari, and J. Ricote, "Texture, Residual Stress and Structural Analysis of Thin Films Using a Combined X-ray Analysis," *Thin Solid Films*, **450**, 34–41 (2004).
[20]D. Chateigner, "Reliability Criteria in Quantitative Texture Analysis With Experimental and Simulated Orientation Distributions," *J. Appl. Crystallogr.*, **38**, 603–11 (2005).
[21]S. Grazulis, D. Chateigner, R. T. Downs, A. F. T. Yokochi, M. Quiros, L. Lutterotti, E. Manakova, J. Butkus, P. Moeck, and A. Le Bail, "Crystallography Open Database – an Open-Access Collection of Crystal Structures," *J. Appl. Crystallogr.*, **42**, 726–9 (2009).
[22]N. C. Popa, "The (*hkl*) Dependence of Diffraction-Line Broadening Caused by Strain and Size for all Laue Groups in Rietveld Refinement," *J. Appl. Crystallogr.*, **31**, 176–80 (1998).
[23]S. Matthies and M. Humbert, "On the Principle of a Geometric Mean of Even-Rank Symmetric Tensors for Textured Polycrystals," *J. Appl. Crystallogr.*, **28**, 254–66 (1995).
[24]G. Pepponi, S. Grazulis, and D. Chateigner, "MPOD: A Material Property Open Database Linked to Structural Information," *Nucl. Instrum. Methods Phys. Res., Sect. B*, **284**, 10–4 (2012), File number 1000314. http://www.materialproperties.org.
[25]S. Nakajima, "The Structure of $Bi_2Te_{3-x}Se_x$," *J. Phys. Chem. Solids*, **24**, 479–85 (1963).
[26]J. Ritter and P. Maruthamuthu, "Synthesis of Polycrystalline Bismuth Telluride by a Metal-Organo Complex Method," *Inorg. Chem.*, **36**, 260–3 (1997).
[27]J. F. Dumas, G. Brun, B. Liautard, J. C. Tedenac, and M. Maurin, "New Contribution in the Study of the Bi_2Te_3–Bi_2Se_3 System," *Thermochim. Acta*, **122**, 135–41 (1987).
[28]G. R. Miller, C. W. Spencer, and C. Y. Li, "Properties of Bi_2Te_3–Bi_2Se_3 Alloys," *J. Appl. Phys.*, **34**, 1398–400 (1963).
[29]V. Perez, C. Tirado, and J. L. Adouby, "X-ray Diffraction and 119Sn Mössbauer Spectroscopy Study of a New Phase in the Bi2Se3−SnSe System: SnBi4Se7," *Inorg. Chem.*, **38**, 2131–5 (1999).
[30]Y. Ma, Q. Hao, B. Poudel, Y. Lan, B. Yu, D. Wang, G. Chen, and Z. F. Ren, "Enhanced Thermoelectric Figure of Merit in p-Type Nanostructured Bismuth Antimony Telluride Made From Elemental Chunks," *Nano Lett.*, **8**, 2580–4 (2008).
[31]Y. Lan, B. Poudel, Y. Ma, D. Wang, M. S. Dresselhaus, G. Chen, and Z. F. Ren, "Structure Study of Bulk Nanograined Thermoelectric Bismuth Antimony Telluride," *Nano Lett.*, **9**, 1419–22 (2009).
[32]A. Goswami and S. S. Koli, "Semiconducting Properties of Bi_2Te_3 and Bi_2Se_3 Films," *Indian J. Pure Appl. Phys.*, **7**, 166–9 (1969).
[33]V. Damodara Das and N. Soundararajan, "Size and Temperature Effects on the Thermoelectric Power and Electrical Resistivity of Bismuth Telluride Thin Films," *Phys. Rev. B*, **37**, 4552–9 (1988). □